applied sciences

MDPI

Article

Design of a Parallel Quadruped Robot Based on a Novel Intelligent Control System

Mingying Li, Zhilei Liu, Manfu Wang, Guibing Pang and Hui Zhang *

School of Mechanical Engineering and Automation, Dalian Polytechnic University, Dalian 116034, China; limy@dlpu.edu.cn (M.L.); liuzhilei_article@163.com (Z.L.); lzl1663063193@163.com (M.W.); pangguibingsx@163.com (G.P.)
* Correspondence: zh1226419340@163.com

Abstract: In order to make a robot track a desired trajectory with high precision and steady gait, a novel intelligent controller was designed based on a new mechanical structure and optimized foot trajectory. Kinematics models in terms of the D-H method were established to analyze the relationship between the angle of the driving joint and the foot position. Inspired by a dog's diagonal trot on a flat terrain, foot trajectory planning in the swing and support phases without impact were fulfilled based on the compound cycloid improved by the Bézier curve. Both the optimized cascade proportional–integral–derivative (PID) control system and improved fuzzy adaptive PID control system were applied to realize the stable operation of a quadruped robot, and their parameters were optimized by the sparrow search algorithm. The convergence speed and accuracy of the sparrow search algorithm were verified by comparing with the moth flame optimization algorithm and particle swarm optimization algorithm. Finally, a co-simulation with MATLAB and ADAMS was utilized to compare the effects of the two control systems. The results of both displacement and velocity exhibit that the movement of a quadruped bionic robot with fuzzy adaptive PID control systems optimized by the sparrow search algorithm possessed better accuracy and stability than cascade PID control systems. The motion process of the quadruped robot in the co-simulation process also demonstrates the effectiveness of the designed mechanical structure and control system.

Keywords: quadruped bionic robot; kinematics; trajectory planning; PID controller; sparrow search algorithm

Citation: Li, M.; Liu, Z.; Wang, M.; Pang, G.; Zhang, H. Design of a Parallel Quadruped Robot Based on a Novel Intelligent Control System. *Appl. Sci.* **2022**, *12*, 4358. https://doi.org/10.3390/app12094358

Academic Editor: Augusto Ferrante

Received: 23 March 2022
Accepted: 23 April 2022
Published: 25 April 2022

1. Introduction

Quadruped robots have received extensive research because of their excellent stability and carrying capacity [1,2], which are less complicated than the hexapod and eight-legged robots [3,4]. These advantages lead to the acceptance of quadruped robots in various working environments, both on rugged and flat ground [5]. The legs are the key component determining the application performance of the quadruped robots. Therefore, many studies have focused on the design of mechanical structure, gait planning, and motion control algorithm to optimize the kinematic performance of the legs.

The mechanical structures of the legs of quadruped robots are mainly divided into series and parallel forms. With respect to the study on the series structure of the robot's legs, Poulakakis et al. [6] developed telescopic column legs using springs to reduce weight and inertia, but this led to a reduction in load capacity. Wensing et al. [7] constructed articulated legs with offset-arranged joints to obtain a larger range of motion during the movement of a robot. Li et al. [8] designed articulated legs using a two-link mechanism composed of a hip flexion joint and a knee joint to simplify the mechanical structure. As mentioned above, the robot's legs of the series structure are simple and have a large working space, but also have the disadvantages of low load capacity, complicated control systems, and high cost. These shortcomings are usually addressed using parallel structural legs.

Kau et al. [9] developed Stanford Doggo with the legs of a parallel four-link mechanism to achieve eight-degree-freedom movement with high speed and load capacity performances. Unfortunately, the two motors located in one joint resulted in reduced stability during motion from friction. Simultaneously, a great deal of effort has been made to improve the stability and rhythm of the gait. Methods of static stability margin (SSM) [10] and central mode processor (CPG) [11–15] were adopted to plan the gait of quadruped robots. In particular, gait trajectory planning based on bionics methodology has recently become a hot topic [16]. Moreover, a control strategy based on structure design also plays an important role in completing the prescribed gait. A proportional–integral–differential (PID) controller was used to control the robot motion with a predetermined, trajectory to achieve small errors [17–20]. To ensure that the controller has acceptable performance, Shabnam et al. used fuzzy systems, and these gains were adaptively tuned for the best performance of the robot against uncertainties in system parameters, external disturbances, and measurement noises [21,22]. However, the control system is complicated. Some more effective and novel swarm intelligence optimization algorithms, such as the Particle Swarm Optimization algorithm [23], Genetic algorithm [24], and Fruit Fly algorithm [25], have emerged for the parameter optimization of a control strategy. Among them, the sparrow search algorithm (SSA) [26] had fewer parameters and stronger robustness compared with other algorithms; thus, it was used to optimize the controller in this study.

This paper aims to solve the problem of quadruped robot walking forward with low accuracy and stability; thus, a quadruped robot with a new mechanical structure, optimized foot trajectory and a novel intelligent control system was designed. The quadruped robot was designed with a five-link leg structure to mimic a dog's diagonal trot. Each leg was a parallel five-link structure with two degrees of freedom, which leads to more even force distribution on the mechanical structure and more carrying capacity. In addition, two joint motors were used to drive two independent kinematic chains simultaneously to reduce kinematic errors. To determine the relationship between the foot position and the angle of the driving joint, the D-H method was used to analyze the kinematics model of the robot's leg. Foot trajectory planning was also completed for decreasing impact force of the robot in the process of movement. Cascade PID controllers and fuzzy adaptive PID controllers were designed according to the mechanical structure and motion form. These controllers were optimized using SSA to find the optimal parameters. The performance of the two control systems was compared through two MATLAB/ADAMS co-simulation experiments.

2. Materials and Methods

2.1. The Mechanical Structure and Kinematics Analysis

2.1.1. The Mechanical Structure

A parallel five-link quadruped robot with eight degrees of freedom was designed as shown in Figure 1a. The leg structure illustrated in Figure 1b is a parallel five link with two degrees of freedom, with a hip joint and a knee joint. The leg was driven by two brushless DC motors located in the hip joint. Considering that quadruped robots have the same motion mechanism between the four legs, which have the same running actions except for time intervals, only the single-leg analysis was carried out in the kinematics analysis of the robot leg structure.

Figure 1c displays the schematic diagram of the parallel five link with two degrees of freedom. L_1, L_2, L_3, L_4 and L_5 represent the link lengths. O_{11} and O_{21} are the hip joints of the robot, and O_3 is the position of the foot. The link coordinate systems are independently established at the center of the frame and the joint of the two links.

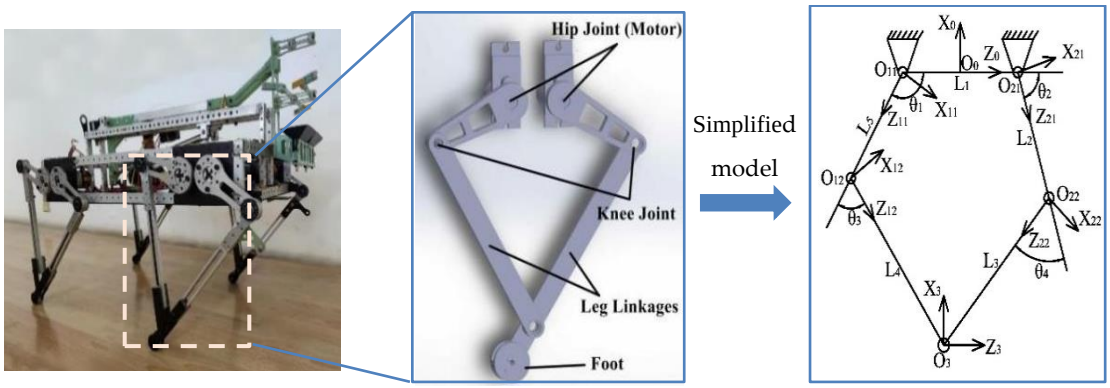

Figure 1. Model building of quadruped robot, (**a**) mechanism schematic of quadruped robot, (**b**) model of quadruped robot with single leg, (**c**) single-leg kinematics model of quadruped robot.

2.1.2. Kinematics Analysis

The D-H method [27] was used to establish the kinematics model of the robot legs. The relationship between the foot position and the angle of the driving joint was obtained.

The D-H method solves the various motion states of the joint when the robot foot moves to the specified position, and it has a wider application range than the geometric method.

The reference coordinate system $\{X_0O_0Z_0\}$ was established at the center of the frame. The ranges of angles between the two links shown in Figure 1c were $\theta_1 \in [-180°, 0]$, $\theta_2 \in [-180°, 0]$, $\theta_3 \in [0, 180°]$, and $\theta_4 \in [-180°, 0]$.

According to Figure 1c, the parameters of both the right and left branches are separately exhibited in Tables 1 and 2.

Table 1. Right branch parameters.

Joint (O_{1i})	α_{i-1}/°	L_i/mm	d_i/mm	θ_i/°
1 (O_{21})	0	$-L_1/2$	0	θ_2
2 (O_{22})	0	L_5	0	θ_4
3 (O_3)	0	L_4	0	$-\theta_2$–θ_4

Table 2. Lift branch parameters.

Joint (O_{1i})	α_{i-1}/°	L_i/mm	d_i/mm	θ_i/°
1 (O_{11})	0	$L_1/2$	0	θ_1
2 (O_{12})	0	L_2	0	θ_3
3 (O_3)	0	L_3	0	$-\theta_2$–θ_4

In Tables 1 and 2, suppose that the current coordinate system is $\{i\}$:

α_{i-1}: the angle of rotation $\{i-1\}$ from the position of Y_{i-1} axis to the position of Y_i axis about X_{i-1} axis;

L_i: the distance from the position of $\{i-1\}$ from the position of Y_{i-1} to the position of Y_i along the X_{i-1} axis;

d_i: the distance from the position of $\{i-1\}$ from X_{i-1} to X_i along the Y_i axis;

θ_i: the angle of rotation $\{i-1\}$ from X_{i-1} to X_i axis position about Y_i axis.

If the current coordinate system is $\{i\}$, when the coordinate system $\{i\}$ is rotated and translated to coincide with $\{i-1\}$, the position of $\{i\}$ in $\{i-1\}$ is described as:

$$\begin{aligned} {}^{i-1}_{i}T &= Rot(x,\alpha_{i-1})\cdot Trans(a_{i-1},0,0)\cdot Rot(y,\theta_i)\cdot Trans(0,d_i,0) \\ &= \begin{bmatrix} c\theta & 0 & s\theta & a_{i-1} \\ s\alpha_{i-1}s\theta & c\alpha_{i-1} & -s\alpha_{i-1}c\theta & d_i c\alpha_{i-1} \\ -c\alpha_{i-1}s\theta & s\alpha_{i-1} & c\alpha_{i-1}c\theta & d_i s\alpha_{i-1} \\ 0 & 0 & 0 & 1 \end{bmatrix} \end{aligned} \tag{1}$$

where $s\theta$ represents $\sin\theta$, and $c\theta$ represents $\cos\theta$, and these abbreviated forms are also applied in the following context.

For the kinematics analysis of the right branch, the parameters in Table 1 are substituted into (1) to obtain each transformation matrix:

$${}^{0}_{11}T = \begin{bmatrix} c\theta_1 & 0 & s\theta_1 & \frac{L_1}{2} \\ 0 & 1 & 0 & 0 \\ -s\theta_1 & 0 & c\theta_1 & 0 \\ 0 & 0 & 0 & 1 \end{bmatrix} \tag{2}$$

$${}^{11}_{12}T = \begin{bmatrix} c\theta_3 & 0 & s\theta_3 & L_2 \\ 0 & 1 & 0 & 0 \\ -s\theta_3 & 0 & c\theta_3 & 0 \\ 0 & 0 & 0 & 1 \end{bmatrix} \tag{3}$$

$${}^{12}_{3}T = \begin{bmatrix} c(\theta_1+\theta_3) & 0 & -s(\theta_1+\theta_3) & L_3 \\ 0 & 1 & 0 & 0 \\ s(\theta_1+\theta_3) & 0 & c(\theta_1+\theta_3) & 0 \\ 0 & 0 & 0 & 1 \end{bmatrix} \tag{4}$$

The transformation matrix of the coordinate system relative to the reference coordinate system for each link is obtained as follows:

$${}^{0}_{12}T = {}^{0}_{11}T\,{}^{11}_{12}T = \begin{bmatrix} c(\theta_1+\theta_3) & 0 & s(\theta_1+\theta_3) & L_2c\theta_1+\frac{L_1}{2} \\ 0 & 1 & 0 & 0 \\ -s(\theta_1+\theta_3) & 0 & c(\theta_1+\theta_3) & -L_2s\theta_1 \\ 0 & 0 & 0 & 1 \end{bmatrix} \tag{5}$$

$${}^{0}_{3}T = {}^{0}_{11}T\,{}^{11}_{12}T\,{}^{12}_{3}T = \begin{bmatrix} 1 & 0 & 0 & L_3c(\theta_1+\theta_3)+L_2c\theta_1+\frac{L_1}{2} \\ 0 & 1 & 0 & 0 \\ 0 & 0 & 1 & -L_3s(\theta_1+\theta_3)-L_2s\theta_1 \\ 0 & 0 & 0 & 1 \end{bmatrix} \tag{6}$$

In the model, the direction of the terminal coordinate system is consistent with that of the reference coordinate system (without rotation); therefore, the transformation matrix P of the terminal coordinate system with respect to the reference coordinate system is shown (7).

$$P = \begin{bmatrix} 1 & 0 & 0 & Px \\ 0 & 1 & 0 & 0 \\ 0 & 0 & 1 & Pz \\ 0 & 0 & 0 & 1 \end{bmatrix} \tag{7}$$

According to the principle that the position matrix of the foot in the reference coordinate system and the matrix of the terminal coordinate system ($\{X_3O_3Z_3\}$) after coordinate system transformation should be equal, (8)–(10) are established:

$$\begin{cases} P = {}^{3}_{0}T = {}^{0}_{11}T{}^{11}_{12}T{}^{12}_{3}T \\ {}^{0}_{11}T^{-1}P = {}^{0}_{11}T^{-1}{}^{3}_{0}T \\ {}^{0}_{12}T^{-1}P = {}^{0}_{12}T^{-1}{}^{3}_{0}T \end{cases}$$

Write Equations (11)–(15) according to Equations (8)–(10).

$$Px \times c(\theta_1 + \theta_3) - (\frac{L_1}{2} \times c(\theta_1 + \theta_3) + \ldots\ldots - L_3\Big(c^2(\theta_1 + \theta_3) - s^2(\theta_1 + \theta_3)\Big) = 0 \quad (11)$$

$$Pz \times c(\theta_1 + \theta_3) - (\frac{L_1}{2} \times s(\theta_1 + \theta_3) + \ldots\ldots + Px \times s(\theta_1 + \theta_3) = 0 \quad (12)$$

$$Pz \times c\theta_1 - Px \times s\theta_1 - \frac{L_1}{2} \times s\theta_1 = L_3 \times s\theta_3 \quad (13)$$

$$L_3c(\theta_1 + \theta_3) + L_2c\theta_3 + \frac{L_1}{2} = Px \quad (14)$$

$$Px \times c\theta_1 - Pz \times s\theta_1 - \frac{L_1}{2} \times c\theta_1 = L_3 \times c\theta_3 + L_2 \quad (15)$$

The solutions of $s\theta_1$ and $c\theta_1$ within a certain range are obtained:

$$s\theta_1 = \frac{\left(\frac{L_1}{2} - Px + L_3\right) \times \left(a + Pz \times \sqrt{b - {L_2}^2}\right)}{Pz \times b - \frac{L_2}{Pz}} \quad (16)$$

$$c\theta_1 = \frac{a + Pz \times \sqrt{b - {L_2}^2}}{b} \quad (17)$$

where, $a = L_1/2 \times L_2 - Px \times L_2 + L_2 \times L_3$, $b = Px^2 - 2Px \times L_1/2 - 2Px \times L_3 + Pz^2 + (L_1/2)^2 + L_1 \times L_3 + {L_3}^2$.

The double variable arctangent function is expressed as:

$$\theta_1 = \arctan2(s\theta_1, c\theta_1), \theta_1 \in [-\pi, \pi]. \quad (18)$$

The solution process of the left branch is exactly the same as that of the right branch; thus, it will not be described here.

With the same approach, θ_2 could be expressed as:

$$s\theta_2 = \frac{Pz \times \left(L_5 + \sqrt{c}\right)}{2 \times d} \quad (19)$$

$$c\theta_2 = \frac{\left(Px + \frac{L_1}{2}\right) \times \left(L_5 + \sqrt{c}\right)}{2 \times d} \quad (20)$$

where $c = -4 \times Px^2 - 8 \times Px \times \frac{L_1}{2} - 4 \times Pz^2 + {L_5}^2 - 4 \times \left(\frac{L_1}{2}\right)^2, d = Px^2 + 2 \times Px \times \left(\frac{L_1}{2}\right) + Pz^2 + \left(\frac{L_1}{2}\right)^2$.

Therefore,

$$\theta_2 = \arctan2(s\theta_2, c\theta_2), \theta_2 \in [-\pi, \pi]. \quad (21)$$

The angle of the driving joint is calculated in real time using (18) and (21) when the geometric parameters of the leg mechanism and foot position are known, which lay a foundation for the subsequent foot planning and control system design.

2.2. Planning and Improvement of Foot Trajectory

The foot trajectory of a quadruped robot in a diagonal trot gait is planned and designed. The zero-impact compound cycloid trajectory planning algorithm is applied, and it is improved via the Bézier curve.

2.2.1. Foot Trajectory Planning

Aiming to minimize the impact forces when the support phase and the swing phase exchange, the displacement and velocity curves should be smooth. Simultaneously, in order to reduce the dragging phenomenon during the motion of the quadruped robot, a compound cycloid is selected as the foot trajectory of a quadruped robot, which is described as follows (22):

$$\begin{cases} X = S\left[\frac{t}{T_m} - \frac{1}{2\pi}\sin\left(\frac{2\pi t}{T_m}\right)\right] \\ Z = H\left[\frac{1}{2} - \frac{1}{2}\cos\left(\frac{2\pi t}{T_m}\right)\right] \end{cases} \tag{22}$$

where S is the step length, H is the foot height and T_m is the time of swing phase.

2.2.2. Improved Trajectory Planning Based on Bézier Curve

In (22), S representing the stride length is set to 50 mm, H representing the leg lifting height is 20 mm, and the periodic time of the swing phase is 0.5 s. The support phase was acquired to move 50 mm in the X-direction. The results are presented in Figure 2a.

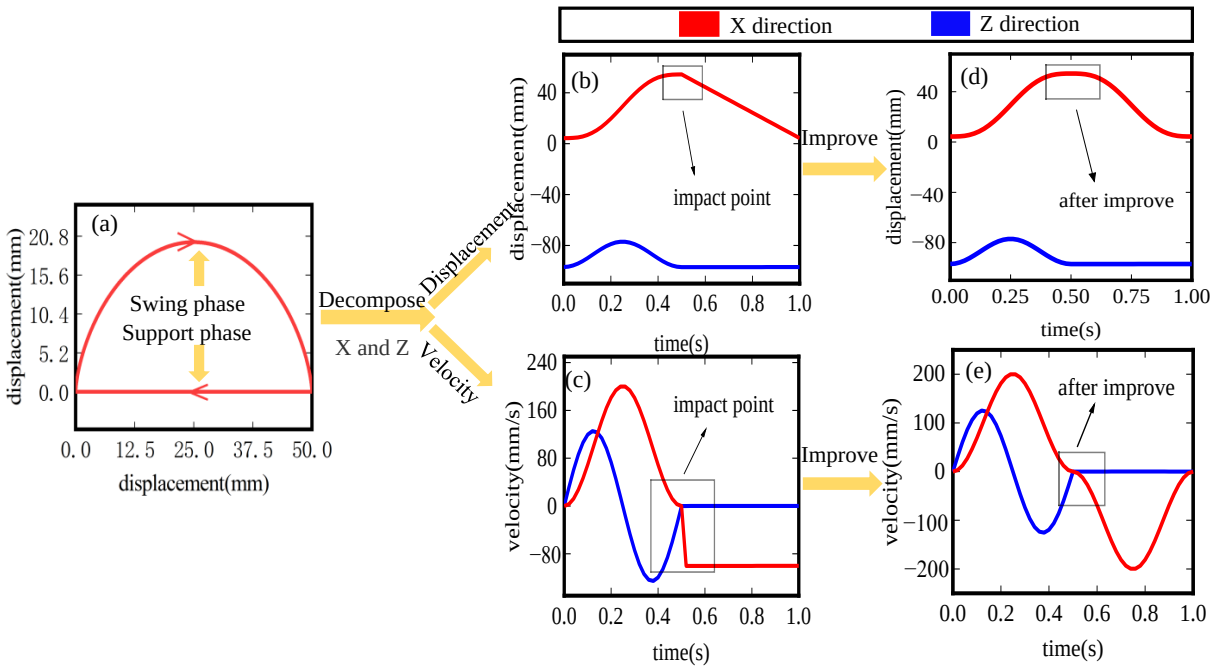

Figure 2. Schematic diagram of motion curve decomposition and optimization of quadruped robot, (**a**) zero-impact foot trajectories in the swing and support phases, (**b**) zero-impact displacement trajectory before the improvement, (**c**) zero-impact velocity trajectory before the improvement, (**d**) zero-impact displacement trajectory after the improvement, and (**e**) zero-impact velocity trajectory after the improvement.

The trajectory cycle of the foot was set as 1 s. The velocity of the support phase was initially designed such that it did not change with time on the premise of sufficient displacement. As a result, the corresponding displacement curves of the foot are described in Figure 2b, and the corresponding velocity curves of foot are illustrated in Figure 2c.

The curves of Figure 2b,c are smooth at 0–0.5 and 0.5–1 s, respectively, but the foot speed value surges and the acceleration increase when the swing phase is exchanged into the support phase, which leads to the foot receiving a large impact.

A Bézier curve under the action of four points was used to improve the motion curve of the support phase to maintain the stability of the robot.

The parameter form of Bézier curve is exhibited in (23).

$$B(t) = \sum_{i=0}^{n} \begin{pmatrix} n \\ i \end{pmatrix} Pi(1-t)^{n-i} t^i \tag{23}$$

where Pi is the control point, and n is the number of control points.

The improved foot trajectory by Bézier curve is presented in Figure 2d,e.

The Bézier curve has many characteristics, such as recursion and geometric invariance, which ensure the continuity and stability of the foot motion of a quadruped robot.

2.3. Control System

Superior controller design is an essential procedure to reduce the operational instability of a joint motor. For this reason, two promising control systems including the cascade PID control system and the fuzzy adaptive PID control system are designed and optimized, respectively, in this section. Each control system requires eight controllers to complete the planned actions.

2.3.1. Cascade PID Controller

A cascade PID controller is used to control the motor with closed-loop servo to rotate the drive joint to rotate with a small error compared to the desired trajectory. The external loop of the cascade PID controller is a position closed loop, and the inner loop is velocity closed loop as presented in Figure 3. The output of the outer loop is the input of the inner loop, and the inner loop sends control parameters to the motor, and the angular displacement and angular velocity of the motor are separately sent to the external and inner loops as feedback signals.

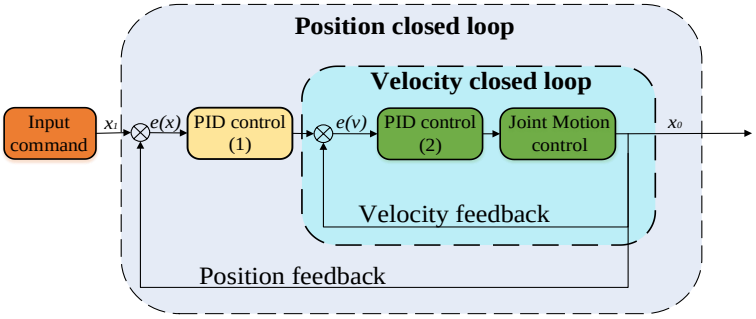

Figure 3. Cascade PID controller control block diagram.

The parameters for each cascade PID controller are manually determined based on the characteristics of the control system before the robot system operation. The determined parameters to the cascade PID controller are input before the robot system operation. Therefore, the cascade PID parameters are not changed in the process of robot system operation. The position closed loop and velocity closed loop have the same control structure, and each cascade PID controller has six parameters, which are two proportional gains (k_p), two integral gains (k_i), and two differential gains (k_d).

PID controller equation:

$$u_{PID}(t) = k_p e(t) + k_I \int e(t)dt + k_D \dot{e}(t) \tag{24}$$

where $e(t)$ is the error between the reference and actual values. The reference value is the expected input value, and the actual value is the actual output response.

The parameters setting of the cascade PID controller directly affects the response of the foot to control. Because the PID parameters are fixed in the system operation, the system

operation will be easily interfered by external factors; further improvements are needed to improve accuracy and stability.

2.3.2. Fuzzy Adaptive PID Controller

The fuzzy adaptive PID controller makes the parameters of the PID controller able to adjust adaptively in the process of system operation, such that the control system has higher precision to achieve the purpose of control. The control system block diagram is illustrated in Figure 4.

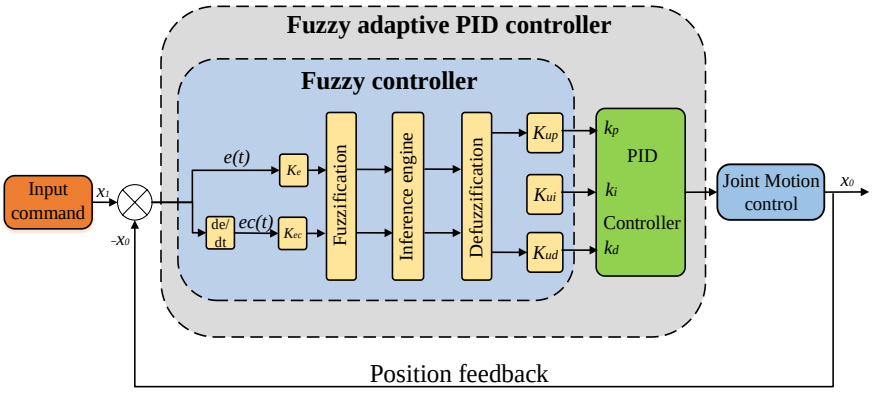

Figure 4. Fuzzy adaptive PID controller control block diagram.

Each fuzzy controller has two inputs, the error $e(t)$ and the rate of change of the error $ec(t)$. After the input is fuzzified, fuzzy reasoning is carried out by inference engine according to the fuzzy rules, and the outputs of the fuzzy controller are obtained after the value of fuzzy reasoning enter the defuzzification. The fuzzy controller has three outputs to adjust the three parameters Δk_p, Δk_i and Δk_d, respectively.

The quantification factor of the $e(t)$ and $ec(t)$ separately is K_e and K_{ec}. K_e and K_{ec} are empirically 1 and 0.5, respectively. The universe of discourse of inputs membership functions is $[-6, 6]$, and the universe of discourse of outputs membership functions is $[0, 6]$, The membership functions select seven language variables, {NL, NM, NS, ZE, PS, PM, PL}. As exhibited in Figure 5, the triangular membership function is designed. The design of fuzzy rules is visually shown in Figure 6.

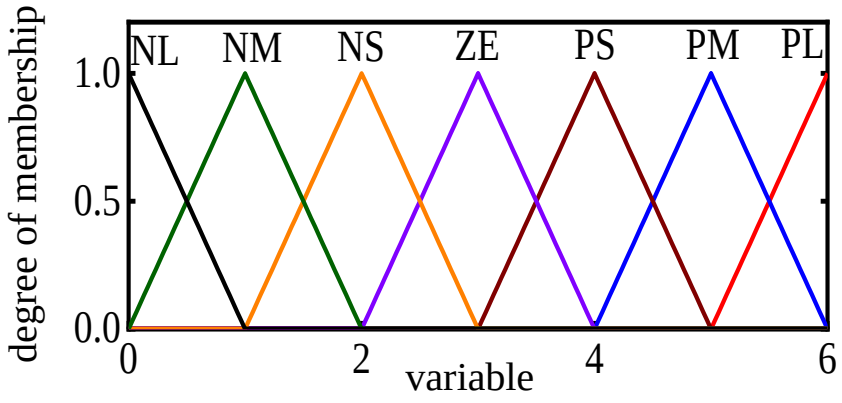

Figure 5. Membership function graph.

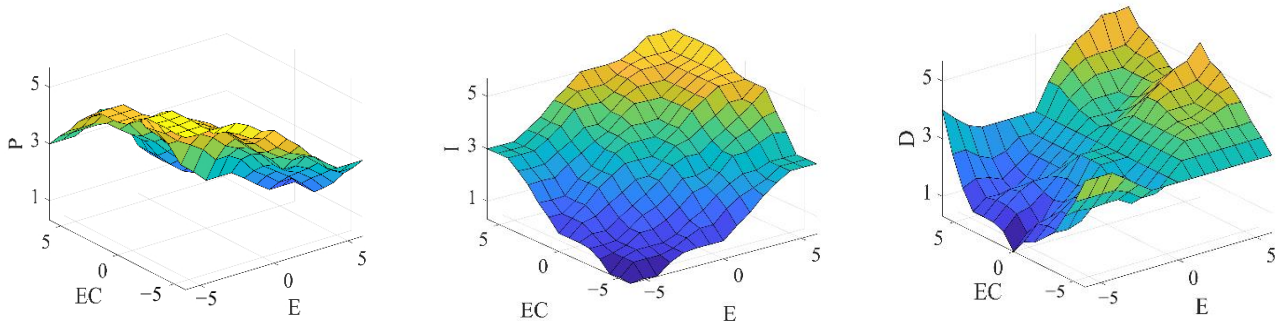

(**a**) (**b**) (**c**)

Figure 6. Schematic diagram of fuzzy rules: (**a**) fuzzy rule diagram of Δk_p; (**b**) fuzzy rule diagram of Δk_i; (**c**) fuzzy rule diagram of Δk_d.

2.3.3. The Optimization of the Controller

The SSA is adopted to optimize two control systems because of its fast convergence speed and good accuracy. There are three species of sparrow individuals in the sparrow population, namely discoverer, subscriber and watchman. The discoverers are responsible for finding food and providing directions for subscribers. The subscribers are responsible for tracking the discoverers and searching for food around them. The watchmen are the sparrow individuals located in the periphery of the sparrow population, responsible for monitoring the environment and issuing warnings.

First, the SSA parameters and all the candidate parameter groups are initialized as listed in Table 3.

Table 3. Initialization parameters of SSA.

Parameter Names	Parameter Values
population	100
number of iterations	100
proportion of discoverers	0.6
proportion of subscribers	0.4
proportion of watchmen	0.1

The matrix M of sparrow population initialization is established as (25):

$$M = \begin{bmatrix} x_{1,1} & \cdots & x_{1,m} \\ x_{2,1} & \cdots & x_{2,m} \\ \vdots & \vdots & \vdots \\ \vdots & \vdots & \vdots \\ x_{n,1} & \cdots & x_{n,m} \end{bmatrix} \tag{25}$$

where M matrix represents the candidates of the control system, and n represents the total number of candidate parameter groups. x_{1i} represents the first parameter group, where $i = \{1, 2, \ldots, m\}$, x_{2i} represents the second parameter group, where $i = \{1, 2, \ldots, m\}$, x_{ni} represents the nth parameter group, where $i = \{1, 2, \ldots, m\}$.

The fitness value of each sparrow is calculated as follows by designing the fitness function:

$$F = \begin{bmatrix} f\left(\begin{bmatrix} x_{1,1} & \cdots & x_{1,m} \end{bmatrix}\right) \\ f\left(\begin{bmatrix} x_{2,1} & \cdots & x_{2,m} \end{bmatrix}\right) \\ \vdots \\ \vdots \\ f\left(\begin{bmatrix} x_{n,1} & \cdots & x_{n,m} \end{bmatrix}\right) \end{bmatrix} \tag{26}$$

where F represents the fitness function matrix, and f represents the fitness value of each sparrow.

Candidate parameter groups are arranged in ascending order in terms of the fitness value after the fitness function values matrix of the parameter groups are obtained. Each parameter group in the M matrix is input into the controller in this step.

The PID parameter values corresponding to each discoverer are obtained by the following formula in the optimization process:

$$X_{i,j}^{t+1} = \begin{cases} X_{i,j}^{t} \cdot exp(-\frac{i}{\alpha \cdot item_{max2}}) & if \quad R_2 < ST \\ X_{i,j}^{t} + Q \cdot L & if \quad R_2 \geq ST \end{cases} \tag{27}$$

where t is the number of current iterations, and $item_{max}$ is the number of iterations of the algorithm. $\alpha \in (0, 1)$ is a random number. $R_2 \in [0, 1]$. Q is a random number that follows a normal distribution. L is a $1 \times d$ matrix where all the entries are 1.

The parameter values of the PID controller corresponding to the subscribers are described as:

$$X_{i,j}^{t+1} = \begin{cases} Q \cdot exp(\frac{X_{worst} - X_{i,j}^{t}}{i^2}) & if \quad i > n/2 \\ X_{P}^{t+1} + \left| X_{i,j}^{t} - X_{P}^{t+1} \right| \cdot A^{+} \cdot L & otherwise \end{cases} \tag{28}$$

where X_P is the parameter group with the highest order of fitness function, and X_{worst} is the parameter group with the lowest order of fitness function. A is the X_{worst} matrix in which each element is randomly assigned to either 1 or -1, and $A^{+} = A^{\mathrm{T}}(AA^{\mathrm{T}})^{-1}$.

The initial position of the watchmen is determined randomly, and the position update in the iteration process is described as:

$$X_{i,j}^{t+1} = \begin{cases} X_{best}^{t} + \beta \cdot \left| X_{i,j}^{t} - X_{best}^{t} \right| & if \quad f_i > f_g \\ X_{i,j}^{t} + K \cdot \left(\frac{\left| X_{i,j}^{t} - X_{worst}^{t} \right|}{(f_i - f_w) + \varepsilon} \right) & if \quad f_i = f_g \end{cases} \tag{29}$$

where X_{best} is the current global optimal position. β is the step-size control parameter. $K \in [-1, 1]$. f_g and f_w are the first and last digits of the fitness function, respectively. ε is a small constant that makes the divisor nonzero.

In the cascade PID control process, it is necessary to optimize six parameters of cascade PID by SSA because manual adjustment of PID parameters is time-consuming and laborious, and high precision cannot be achieved. The parameters optimized by SSA will be input to the cascade PID controller before the robot operation; thus, the cascade PID parameters remain unchanged during the robot operation. The proportion factor of the fuzzy controller will directly affect the control precision of the fuzzy adaptive PID controller in the control process. Therefore, it is novel and important to choose SSA to optimize the proportion factor in this paper. The flow chart of the control system is shown in Figure 7.

Figure 8a exhibits the comparison among SSA—the moth flame optimization algorithm (MFO) and particle swarm optimization algorithm (PSO) in terms of convergence speed and optimization accuracy when optimizing cascade PID controller. Figure 8b shows the comparison between SSA and other algorithms in terms of convergence speed and optimization accuracy when optimizing the fuzzy adaptive PID controller. It is proven that SSA has faster convergence speed and better optimization accuracy under the same conditions.

The optimization results of cascade PID controller parameters using three different algorithms are shown in Table 4, and the optimization results of fuzzy adaptive PID controller proportion factor are shown in Table 5.

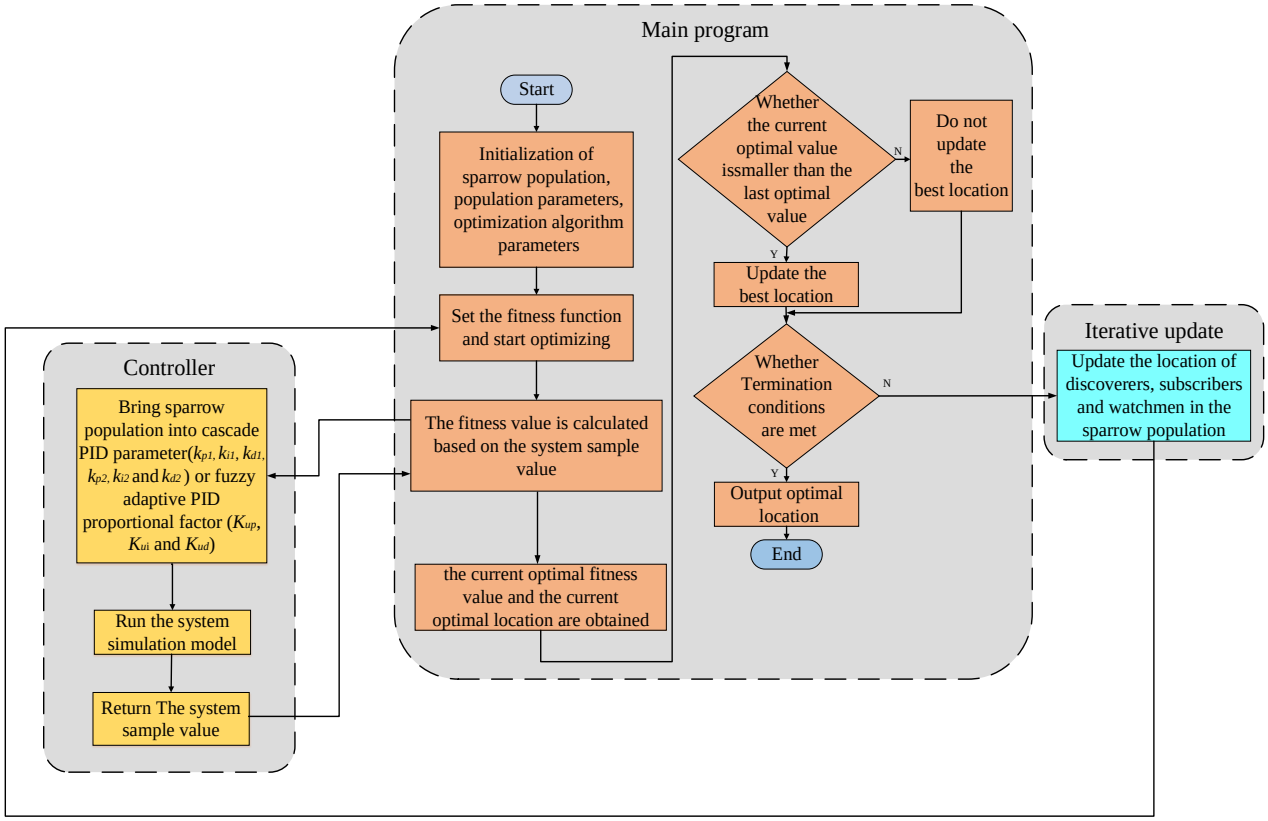

Figure 7. Flow chart of the controller parameters optimized using SSA.

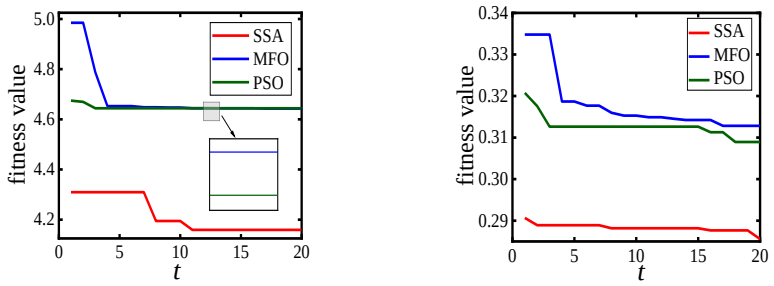

(**a**) (**b**)

Figure 8. Convergence rate curve of the fitness of angular displacement during the optimization process, (**a**) optimize the cascade PID controller, (**b**) optimize the fuzzy adaptive PID controller.

Table 4. Parameters factor optimization results of fuzzy controller.

Algorithm	k_{p1}	k_{i1}	k_{d1}	k_{p2}	k_{i2}
SSA	20.0000	1.2977	19.8444	5.7473	19.4983
MFO	20.0000	0.0245	20.0000	19.5924	20.0000
PSO	20.0000	0.0000	20.0000	19.2943	0.0149

Table 5. Proportion factor optimization results of fuzzy controller.

Algorithm	K_{up}	K_{ui}	K_{ud}
SSA	19.9936	20.0000	20.0000
MFO	19.5910	0.0000	20.0000
PSO	19.6313	0.0000	20.0000

SSA has good performance in convergence speed and optimization accuracy compared with other algorithms, which is proven by the above results.

Figure 9 demonstrates the comparison between the optimized fuzzy adaptive PID controller and the optimized cascade PID controller using SSA for the desired trajectory. The curve of the optimized fuzzy adaptive PID controller angular displacement is much closer to the desired curve. It is proven that the fuzzy adaptive PID controller is much better than the cascade PID controller in controlling the joint motor.

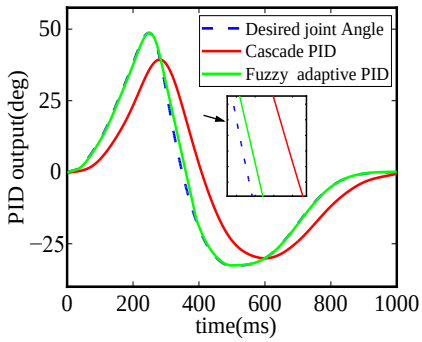

Figure 9. Comparison between the optimized angular displacement input curve and the desired curve.

3. Results and Discussions

The mechanical structure system and two control systems mentioned above were simulated, and the simulation results were analyzed.

Figure 10 depicts the motion state of a single leg and the body for the quadruped robot in forward motion. The red lines represent the left branch, and the yellow lines represent the right branch. The trajectory was improved using the Bézier curve. The black and blue dots represent the motion state of the body centroid and foot centroid, respectively. The crowding level of the dots represents the speed value. A high crowding level indicates low speed. The crowding level of the black dots represents the speed value when entering the swing phase. Owing to the force of friction, the foot pushes the body forward as the foot enters the support phase, and the crowding level of the blue dots represents the speed value when entering the support phase. Figure 10 demonstrates that the quadruped robot has a small impact during phase switching.

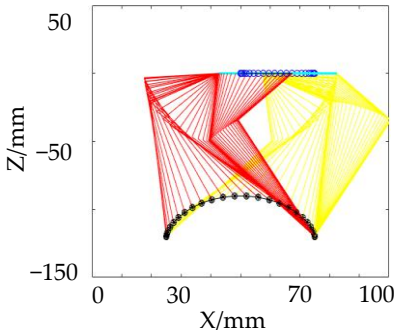

Figure 10. The optimized trajectory of a single leg in one gait cycle.

Subsequently, MATLAB and ADAMS were used to co-simulate the entire movement of the quadruped robot in order to verify the effectiveness of the proposed mechanical structure and control strategy. The input data are transmitted to the interface reserved in ADAMS in the form of a function in MATLAB, and the running state of the quadruped robot is observed in ADAMS in real time. In addition, the post-processing module of ADAMS was used to monitor the robot's foot trajectory, foot velocity, and joint angle in real time, and the data were transmitted to MATLAB for numerical analysis. The simulation results demonstrate the motion state and performance of the robot under different control systems.

For the diagonal gait of the quadruped bionic robot, the state of the left front leg is consistent with that of the right rear leg, and the state of the right front leg is consistent with that of the left rear leg. Therefore, the simulation of the motion state of the left front leg and left rear leg is sufficient to reflect the motion state of the four legs.

The actual motion of the quadruped robot controlled by the cascade PID controller optimized by SSA and the fuzzy adaptive PID controller optimized by SSA is shown in the figure. Figure 11 shows the foot displacement curves of the quadruped robot under the control of a two-control system, and Figure 12 shows the foot velocity curves of the quadruped robot under the control of a two-control system.

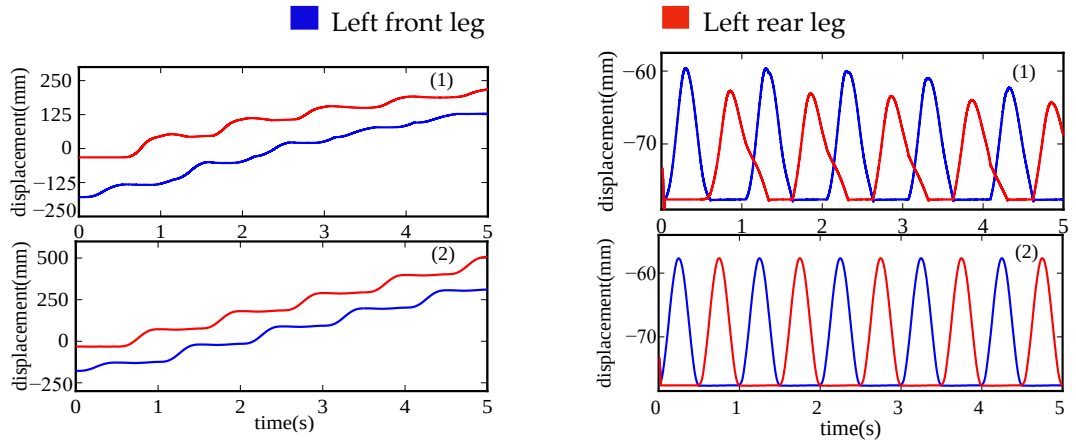

(**a**) X direction (**b**) Z direction

Figure 11. Comparison of foot displacement before and after optimization: (**a**) foot displacement curves in X direction cascade PID (1) and fuzzy adaptive PID (2); (**b**) foot displacement curves in X direction cascade PID (1) and fuzzy adaptive PID (2).

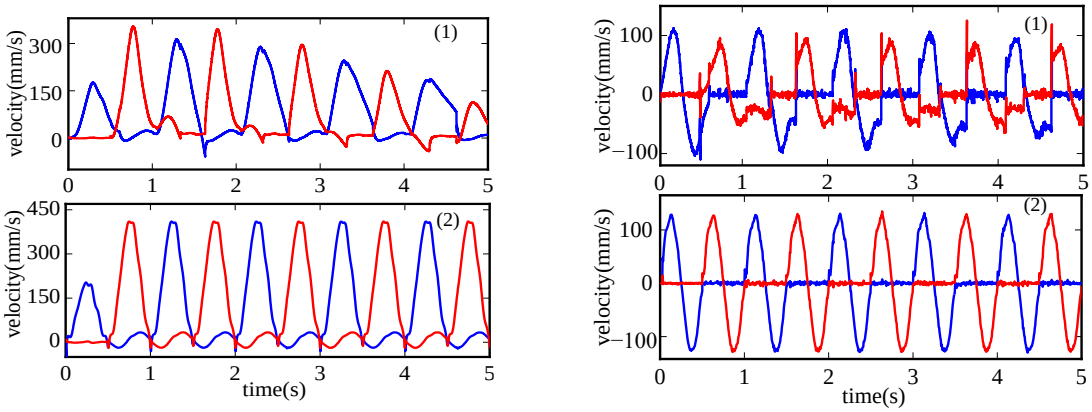

(**a**) X direction (**b**) Z direction

Figure 12. Comparison of foot velocity before and after optimization: (**a**) foot velocity curves in X direction cascade PID (1) and fuzzy adaptive PID (2); (**b**) foot velocity curves in Z direction cascade PID (1) and fuzzy adaptive PID (2).

The simulation results demonstrate that the robot can walk forward using the cascade PID controller. However, there is a large error during the combined motion of the four legs. Furthermore, motors also have transmission errors, which worsen the situation. Because the parameters of the cascade PID cannot change adaptively with the operation of the system, there are some uncertainties in the operation of the robot. The errors become increasingly larger with time, leading to a deterioration in robot stability. Consequently, the tracking of the expected joint angle cannot be fully realized, resulting in a loss of system stability.

Simultaneously, the simulation results also demonstrate that the fuzzy adaptive PID has relatively strong adaptive ability in the quadruped robot to walk stably forward. The swing phase moves 50 mm in the X direction in conformity with the desired trajectory presented in Figure 2, and the support phase supports the robot body forward by 50 mm owing to friction. Therefore, the foot moves forward 100 mm each time, except for the first step, and the foot velocity also increases compared with the first step, as described in Figures 11 and 12. The foot displacement and velocity under fuzzy adaptive PID controller conform to the desired trajectory presented in Figure 2c,e. The superiority of the fuzzy adaptive PID controller optimized by SSA in controlling the motion of the quadruped robot was verified.

The simulation process using the cascade PID control system based on SSA to optimize parameters in a complete gait cycle is presented in Figure 13, and the simulation process using the fuzzy adaptive PID control system based on SSA to optimize the proportional factor in a complete gait cycle is presented in Figure 14. The simulation results visually demonstrate that the robot moves forward with higher stability under the fuzzy adaptive PID control. However, the error of the robot movement becomes larger with time under the cascade PID control, leading to an unstable movement. The movements of the four legs are not completely consistent, resulting in the leg drive robot not walking in a straight line.

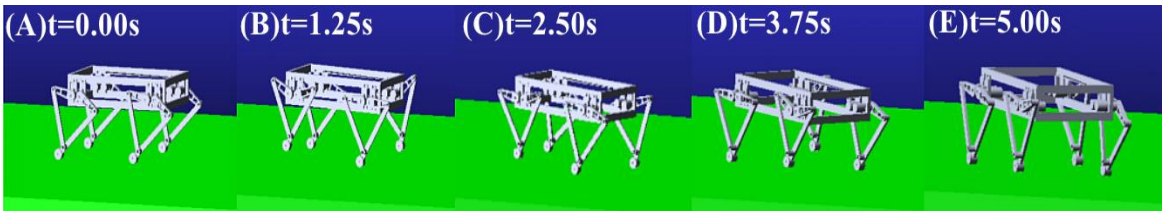

Figure 13. Schematic diagram of simulation process using cascade PID control system in a complete gait cycle.

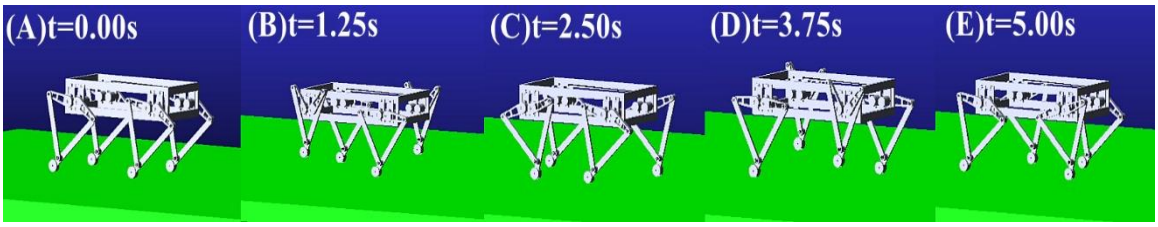

Figure 14. Schematic diagram of simulation process using fuzzy adaptive PID control system in a complete gait cycle.

4. Conclusions

A novel quadruped robot imitating a dog's diagonal trot was developed in this study. To solve the complex motion control problem of a quadruped robot, the mechanical structure of the robot's legs and the corresponding control strategy were designed and optimized.

(1) The mechanical structure of the robot's leg was designed using a parallel five link with two degrees of freedom. The angle function of the leg joint was obtained using the D-H method for kinematics analysis. Moreover, the phase switch with minimum impact during the entire movement process was realized and verified.

(2) The cascade PID control system optimized based on the sparrow search algorithm and the fuzzy adaptive PID control system optimized based on the sparrow search algorithm are used to drive the quadruped robot, and the overall performance of the two control strategies are compared in the simulation. The convergence speed and accuracy of the sparrow search algorithm are verified by comparing with the moth flame optimization algorithm and particle swarm optimization algorithm.

(3) The fuzzy adaptive PID optimized based on the sparrow search algorithm has higher precision and more stable control effect compared with the cascade PID control optimized based on the sparrow search algorithm, which was demonstrated by co-simulation using MATLAB and ADAMS. The simulation results also simultaneously verified that the parallel five link with eight degrees of freedom quadruped robot and its control system provided a reliable solution for the operation of a quadruped robot and provided a reference for other related researchers.

Author Contributions: M.L. designed the project and coordinated the work. Z.L. and M.L. checked and discussed the results and the whole manuscript. H.Z. and M.W. revised the manuscript. G.P. contributed to the discussion of this study. All authors reviewed the manuscript. All authors have read and agreed to the published version of the manuscript.

Funding: This research was funded by the Scientific Research Fund Project of Education Department of Liaoning Province, grant number LJKZ0510. This research was also funded by the Major Project of Liaoning Industrial Research Institute, grant number 2018LY011.

Institutional Review Board Statement: Not applicable.

Informed Consent Statement: Not applicable.

Data Availability Statement: Not applicable.

Acknowledgments: The authors would like to thank the Scientific Research Fund of The Education Department of Liaoning Province for the financial support of the present research project (project code: LJKZ0510). The authors would also like to gratefully acknowledge the Major Project of Liaoning Industrial Research Institute for the financial support of the current research project (project code: 2018LY011).

Conflicts of Interest: The authors declare no conflict of interest.

References

1. Raibert, M.; Blankespoor, K.; Nelson, G.; Playter, R. Bigdog, the Rough-Terrain Quadruped Robot. *IFAC Proc.* **2008**, *41*, 10822–10825. [CrossRef]
2. Wang, L.; Du, W.; Mu, X.; Wang, X.; Xie, G.; Wang, C. A geometric approach to solving the stable workspace of quadruped bionic robot with hand-foot-integrated function. *Robot. Comput.-Integr. Manuf.* **2016**, *37*, 68–78. [CrossRef]
3. Tian, X.; Gao, F.; Qi, C.; Chen, X.; Zhang, D. External disturbance identification of a quadruped robot with parallel–serial leg structure. *Int. J. Mech. Mater. Des.* **2016**, *12*, 109–120. [CrossRef]
4. Zhang, L.; Li, A.; Gao, Z. Modeling and Analysis of Flexible Foot Vibration of Multi-Foot Bionic Robot. In Proceedings of the 2019 IEEE International Conference on Robotics and Biomimetics (ROBIO), Dali, China, 6–8 December 2019; pp. 136–141.
5. Hirose, S.; Kato, K. Study on quadruped walking robot in Tokyo Institute of Technology-past, present and future. *Proc. IEEE Int. Conf. Robot. Autom.* **2000**, *1*, 414–419.
6. Ioannis, P.; James, A.S.; Martin, B. Modeling and Experiments of Untethered Quadrupedal Running with a Bounding Gait: The Scout II Robot. *Int. J. Robot. Res.* **2005**, *24*, 239–256.
7. Patrick, M.W.; Albert, W.; Sangok, S.; David, O.; Jeffrey, L.; Sangbae, K. Proprioceptive Actuator Design in the MIT Cheetah: Impact Mitigation and High-Bandwidth Physical Interaction for Dynamic Legged Robots. *IEEE Trans. Robot.* **2017**, *33*, 509–522.
8. Rong, X.; Li, Y.; Meng, J. Design for several hydraulic parameters of a quadruped robot. *Appl. Math. Inform. Sci.* **2014**, *8*, 2465–2470. [CrossRef]
9. Nathan, K.; Aaron, S.; Natalie, F.; Patrick, S. Stanford Doggo: An Open-Source, Quasi-Direct-Drive Quadruped. In Proceedings of the 2019 International Conference on Robotics and Automation (ICRA), Montreal, QC, Canada, 20–24 May 2019; pp. 6309–6315.
10. Hao, L.; Chen, B.; Liu, Y.; Lu, Y. Guardian Map Approach to Feasible Range of Static Stability Margin of Hypersonic Flight Vehicles with Input Saturation. *Int. J. Aerosp. Eng.* **2020**, *2020*, 8895324.
11. Yu, H.; Gao, H.; Ding, L.; Li, M.; Deng, Z.; Liu, G. Gait Generation With Smooth Transition Using CPG-Based Locomotion Control for Hexapod Walking Robot. *IEEE Trans. Ind. Electron.* **2016**, *63*, 5488–5500. [CrossRef]
12. Xu, H.; Gan, S.; Ren, J.; Wang, B.; Jin, Y. Gait CPG Adjustment for a Quadruped Robot Based on Hopf Oscillator. *J. Syst. Simul.* **2017**, *29*, 3092–3099.
13. Liu, W.; Zhang, C.; Chen, J.; Qi, J. Survey of locomotion control of legged robots inspired by biological concept. *Sci. China Ser. F Inf. Sci.* **2009**, *52*, 1715–1729.
14. Zhong, G.; Chen, L.; Jiao, Z.; Li, J.; Deng, H. Locomotion Control and Gait Planning of a Novel Hexapod Robot Using Biomimetic Neurons. *IEEE Trans. Control Syst. Technol.* **2018**, *26*, 624–636. [CrossRef]

15. Liu, C.; Wang, D.; Chen, Q. Adaptive walking control of biped robots using online trajectory generation method based on neural oscillators. *J. Bionic. Eng.* **2016**, *13*, 572–584. [CrossRef]
16. Alexander, R.M. The Gaits of Bipedal and Quadrupedal Animals. *Int. J. Robot. Res.* **1984**, *33*, 49–59. [CrossRef]
17. Gor, M.M.; Pathak, P.M.; Samantaray, A.K.; Yang, J.M.; Kwak, S.W. Control of compliant legged quadruped robots in the workspace. *Simulation* **2015**, *91*, 103–125. [CrossRef]
18. Zhao, M.; Liu, L.; Wang, J.; Chen, K.; Zhao, J.; Xu, K. Control system design of THBIP-I humanoid robot. In Proceedings of the 2002 IEEE International Conference on Robotics and Automation (Cat. No.02CH37292), Washington, DC, USA, 11–15 May 2002; Volume 3, pp. 2253–2258.
19. Meinard, C.A.; Manuel, C.R. Bipedal robot locomotion using multivariable control. In Proceedings of the TENCON 2009–2009 IEEE Region 10 Conference, Singapore, 23–26 January 2009; pp. 1–6.
20. Moosavian, S.A.A.; Khorram, M.; Zamani, A.; Abedini, H. PD regulated sliding mode control of a quadruped robot. In Proceedings of the 2011 IEEE International Conference on Mechatronics and Automation, Beijing, China, 7–10 August 2011; pp. 2061–2066.
21. Shabnam, S.; Mohammad, F. Fuzzy-backstepping control of quadruped robots. *Intel. Serv. Robot.* **2020**, *13*, 13191–13206.
22. Wu, H.M.; Karkoub, M.; Hwang, C.L. Mixed Fuzzy Sliding-Mode Tracking with Backstepping Formation Control for Multi-Nonholonomic Mobile Robots Subject to Uncertainties. *J. Intell. Robot. Syst.* **2015**, *79*, 73–86. [CrossRef]
23. Wang, D.; Tan, D.; Liu, L. Particle swarm optimization algorithm: An overview. *Soft Comput.* **2018**, *22*, 387–408. [CrossRef]
24. Rahul, B.; Dharani, J. Genetic Algorithm tuned PID Controller for Aircraft Pitch Control. *IJREAM* **2019**, *4*, 303–307.
25. Bezdan, T.; Stoean, C.; Naamany, A.A.; Bacanin, N.; Rashid, T.A.; Zivkovic, M.; Venkatachalam, K. Hybrid Fruit-Fly Optimization Algorithm with K-Means for Text Document Clustering. *Mathematics* **2021**, *9*, 1929. [CrossRef]
26. Xue, J. Research and Application of A Novel Swarm Intelligence Optimization Technique: Sparrow Search Algorithm. Master's Thesis, College of information science and Technology, Donghua University, Shanghai, China, 2020.
27. Liao, W.; Ross, C.; Jonathan, R. An Analytic Approach to Converting POE Parameters into D-H Parameters for Serial-Link Robots. *IEEE Robot. Autom. Lett.* **2019**, *2*, 217.